Enhancement in Thermally Generated Spin Voltage at the Interfaces between Pd and $NiFe_2O_4$ Films Grown on Lattice-Matched Substrates

A. Rastogi,[1] Z. Li,[1,2] A.V. Singh,[1] S. Regmi,[1,2] T. Peters,[3] P. Bougiatioti,[3] D. Carsten né Meier,[3] J.B. Mohammadi,[1,2] B. Khodadadi,[1,2] T. Mewes,[1,2] R. Mishra,[4] J. Gazquez,[5] A.Y. Borisevich,[6] Z. Galazka,[7] R. Uecker,[7] G. Reiss,[3] T. Kuschel,[3,*] and A. Gupta[1,†]

[1] *Center for Materials for Information Technology, The University of Alabama, Tuscaloosa, Alabama 35487, USA*

[2] *Department of Physics & Astronomy, The University of Alabama, Tuscaloosa, Alabama 35487, USA*

[3] *Center for Spinelectronic Materials and Devices, Department of Physics, Bielefeld University, Universitätsstraße 25, Bielefeld 33615, Germany*

[4] *Department of Mechanical Engineering and Materials Science, and Institute of Materials Science and Engineering, Washington University in St. Louis, St. Louis, Missouri 63130, USA*

[5] *Institut de Ciència de Materials de Barcelona, Campus de la UAB, Bellaterra 08193, Spain*

[6] *Materials Science and Technology Division, Oak Ridge National Laboratory, Tennessee 37831, USA*

[7] *Leibniz-Institut für Kristallzüchtung, Max-Born-Str. 2, Berlin 12489, Germany*

(Received 12 July 2019; revised 2 June 2020; accepted 15 June 2020; published 7 July 2020)

Efficient spin injection from epitaxial ferrimagnetic $NiFe_2O_4$ thin films into a Pd layer is demonstrated via spin Seebeck effect measurements in the longitudinal geometry. The $NiFe_2O_4$ films (60 nm to 1 μm) are grown by pulsed-laser deposition on isostructural spinel $MgAl_2O_4$, $MgGa_2O_4$, and $CoGa_2O_4$ substrates with lattice mismatch varying between 3.2 and 0.2%. For the thinner films ($\leq$ 330 nm), an increase in the spin Seebeck voltage is observed with decreasing lattice mismatch, which correlates well with a decrease in the Gilbert damping parameter as determined from ferromagnetic resonance measurements. High-resolution transmission electron microscopy studies indicate substantial decrease of antiphase boundary and interface defects that cause strain relaxation, i.e., misfit dislocations, in the films with decreasing lattice mismatch. This highlights the importance of reducing structural defects in spinel ferrites for efficient spin injection. It is further shown that angle-dependent spin Seebeck effect measurements provide a qualitative method to probe for in-plane magnetic anisotropies present in the films.

DOI: 10.1103/PhysRevApplied.14.014014

I. INTRODUCTION

Efficient conversion of heat to electric energy in thermoelectric materials is an active field of research. Recent studies on the interaction between electron spin and heat flow have created a new area of research in spintronics that is commonly referred to as spin caloritronics [1–7]. The spin Seebeck effect (SSE), which involves generation of spin current through heat flow, is one of the most promising phenomena in the emerging field of spin caloritronics. One approach to efficiently generate spin current is the implementation of a temperature gradient across a magnetic thin film that is perpendicular to the magnetization [8–12]. The spin current is generated parallel to the temperature gradient via the so-called longitudinal spin Seebeck effect (LSSE). It can be injected into a normal metal (Pt, Pd, Au, etc.) electrode and converted into a charge current due to the inverse spin Hall effect (ISHE) [13–15]. The electric field ($\mathbf{E}_{\mathrm{ISHE}}$) generated by the spin current in a normal metal is described by the relationship [11]

$$\mathbf{E}_{\mathrm{ISHE}} = \theta_{\mathrm{SH}} \rho \mathbf{J}_{\mathrm{s}} \times \boldsymbol{\sigma}, \tag{1}$$

where θ_{SH} is the spin Hall angle, ρ is the electrical resistivity of the normal metal, $\mathbf{J}_{\mathrm{s}}$ is spin current density, and $\boldsymbol{\sigma}$ is spin-polarization vector, collinear with the magnetization $\mathbf{M}$.

Using magnetic insulators as a source of spin current has advantages over magnetic metals because unintended effects such as the anomalous Nernst effect can be neglected due to the absence of conduction electrons [16]. In magnetic insulators, magnons, the quanta of spin waves, are the carriers of the generated spin current.

Yttrium iron garnet (YIG) is the most widely studied insulating ferrimagnetic material for LSSE experiments because of its low magnetic coercivity and an extremely low Gilbert damping [17]. Nickel ferrite ($NiFe_2O_4$, NFO) is also a promising candidate for high-frequency applications as its saturation magnetization is much higher than

*tkuschel@physik.uni-bielefeld.de
†agupta@ua.edu

YIG [18]. The use of NFO has further advantages such as the tuning of electrical properties by temperature [12] or by oxygen content [19,20]. However, so far there have been only few reports of LSSE using NFO thin films. The NFO films used in previous studies were deposited by either chemical vapor deposition (CVD) method [12,21–23] or reactive cosputtering [19,24–26] on $MgAl_2O_4$ substrate that has a large lattice mismatch of approximately 3.2%, resulting in the formation of antiphase boundaries (APBs) and interface defects, such as misfit dislocations [27], which limits their usability for device applications. Nevertheless, recent nonlocal magnon spin-transport experiments [26] based on the SSE in sputter-deposited NFO on $MgAl_2O_4$ show that the magnon spin-diffusion length is approximately 3 μm, which is in the same range as for YIG [28]. We have recently shown that with appropriate choice of substrates and growth conditions, NFO thin films can exhibit a saturation magnetization as high as its bulk value, with damping constant and coercivity values comparable to that of YIG [29]. Moreover, Pd is another metal with high spin Hall angle besides Pt, which shows strong potential for spintronics applications [30–32].

In this work, we report on a systematic study of enhancement in the thermally generated ISHE voltage for Pd/NFO films on different (001)-oriented isostructural spinel substrates: $MgAl_2O_4$ (MAO), $MgGa_2O_4$ (MGO), and $CoGa_2O_4$ (CGO) with decreasing lattice mismatch of approximately 3.2, 0.8, and 0.2% with NFO, respectively. The overall microstructure and the interface between the films and substrates have been investigated by high-resolution scanning transmission electron microscopy (STEM), which shows a substantial decrease of APBs and misfit dislocations with decreasing lattice mismatch. For thinner films ($\leq$ 330 nm), the obtained LSSE results correlate well with the damping parameters as determined by ferromagnetic resonance (FMR) measurements. The thermally generated spin-voltage signal increases with decreasing lattice mismatch, whereas the damping parameter decreases.

II. EXPERIMENT

A. Sample preparation and characterization

High-quality epitaxial NFO thin films are deposited using pulsed-laser deposition followed by *in situ* Pd deposition by dc sputtering. For NFO film deposition we use a laser fluence of approximately 1 J/cm^2 in an oxygen environment with a background pressure of 1.3 Pa. The temperature of the substrates is kept constant at 700 °C during film growth. We use three different (001)-oriented spinel substrates, namely MAO, MGO, and CGO. The MAO substrates are purchased commercially (CrysTec GmbH), while the MGO and CGO substrates are prepared from high-quality single crystals, which are grown at the Leibniz Institute for Crystal Growth [33] and then cut and polished by CrysTec GmbH, Berlin, Germany. We investigate films with thicknesses ranging from 60 nm to 1 μm deposited on substrates with a size of 3×5 mm^2. For LSSE measurements, the deposition of NFO film is followed by *in situ* deposition of a 5-nm-thick Pd layer by dc sputtering at 0.7-Pa argon pressure and 20-W power.

The films are structurally characterized using a Philips X′Pert X-ray diffractometer. High-resolution STEM imaging (along the [001] direction) is carried out on some of the samples in an aberration-corrected Nion UltraSTEM™ 200 microscope operating at 200 kV. Two different imaging modes are used, the high-angle annular dark-field (HAADF) and the low-angle annular dark-field (LAADF) imaging modes. The HAADF imaging mode gives rise to the so-called Z contrast, and it is acquired using an annular detector with a high inner collection angle [34]. On the other hand, the LAADF imaging mode is achieved using an annular detector with a smaller inner collection angle, which allows collection of electrons scattered by the strained regions giving rise to different angular distributions of the annular dark-field signal, thus causing extra contrast [35].

The films are magnetically characterized using vibrating sample magnetometry (VSM) in a PPMS® DynaCool™ system (Quantum Design). Room-temperature broadband FMR measurements are performed using a coplanar waveguide to determine the effective Gilbert damping parameter of two films deposited on MGO and CGO substrates and to obtain an estimate of the interface spin-mixing conductance. The FMR measurements are carried out in the in-plane geometry, i.e., with the quasistatic magnetic field applied in the plane of the film.

B. Measurement setup for spin Seebeck effect

We use two methods to normalize the V_{ISHE} signal, namely by heat flux and by thermal gradient. For the heat-flux setup in Bielefeld, we use a calibrated Peltier element clamped between the sample and one of the copper blocks to detect the heat flux as described in Ref. [19,36–38]. The heat-flux method developed by Sola *et al.* helps to improve the reproducibility when determined LSSE coefficients are compared between different setups as well as when remounting samples in the same setup [37,38]. In the thermal-gradient setups in Alabama and Bielefeld, only the sample is sandwiched between two copper blocks [Fig. 1(a)]. The Cu blocks are retained in good thermal contact with Peltier elements for cooling and heating. A thermally conducting and electrically insulating 250-μm-thick SiC spacer is used between the top Pd layer and the upper copper block. For a comparison of different spacers, see Fig. S2 within the Supplemental Material (SM) [39]. For all measurements the spacing between the voltage probes (w) is kept constant, $w \approx 4.8$ mm. The temperature of the lower block is fixed at a base temperature T (room

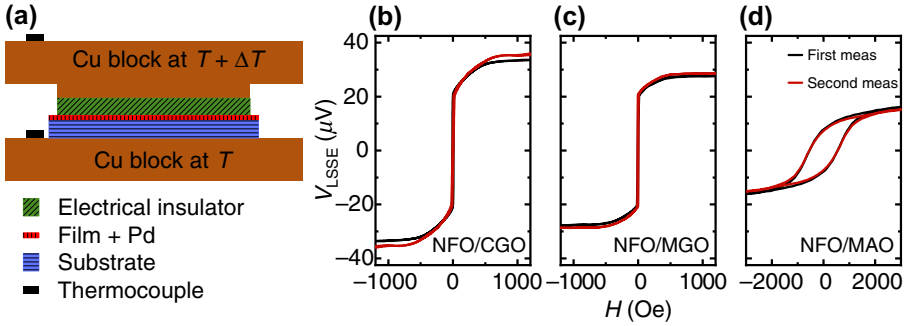

FIG. 1. (a) Schematic of the measurement setup for temperature gradient method. (b)–(d) Reproducibility of the V_{ISHE} signal using a SiC spacer. The measurements are done on 330-nm-thick NFO films deposited on CGO, MGO, and MAO. Black lines show the results of the first measurement, while the red lines show a repeat measurement after remounting the same sample.

temperature, if not stated otherwise), while the temperature of the upper block is varied ($T + \Delta T$) to obtain the desired temperature difference across the sample. A K-type thermocouple is used to measure the temperature at each Cu block. For angular-dependent measurements, the sample is rotated in plane with a manual stage. A helium-based closed-cycle refrigerator is used to carry out the low-temperature measurements. To check the reproducibility of the voltage signal in our setup, we remeasure the same sample repeatedly after remounting, but the voltage signal remains unaffected within the error limit as shown in Figs. 1(b)–1(d). The primary source of error in our measurements is the distance between the electrical contact (approximately 4%). Since the voltage signal remains essentially unchanged after repeated measurements, we can compare results from the same setup using the temperature-difference method in addition to the heat-flux technique. We use the temperature-gradient method for the LSSE measurements of magnetic field and temperature variations. For a quantitative comparison of substrate effects in LSSE, we use the heat-flux method.

III. RESULTS AND DISCUSSION

A. Structural characterization of NFO films on different substrates

All three (001)-oriented substrates, namely CGO, MGO, and MAO, impose a compressive strain on the NFO film, and hence the lattice parameter elongates in the out-of-plane direction. It can be seen in Fig. 2(a) that the film peak position shifts to lower values of 2θ ($2\theta_{bulk} = 43.33^{\circ}$) with increasing lattice mismatch. Omega scans in Fig. 2(b) indicate that epitaxial quality of the films on MGO and CGO are significantly better than the film on MAO. We also perform off-axis XRD scans on few films deposited on three different substrates and calculate the strain in the films, which can be quantified by the parameter $R = (a_f - a_s)/(a_b - a_s)$, with a_f, a_b, and a_s as in-plane lattice parameters of the NFO thin film (measured), NFO bulk (literature), and substrate (single crystal), respectively. Therefore, $R = 1$ for a fully relaxed film and $R = 0$ for a fully strained film. As shown in Fig. 2(c), the films on CGO and MGO substrates have significantly lower values of R than those on MAO and are not fully relaxed with even the thickest films remaining strained. We also use the x-ray reflectivity technique to determine the Pd layer thickness, which is essentially the same (approximately 5.0 ± 0.4 nm) for all the samples.

Low-magnification STEM images of the films grown on CGO, MGO, and MAO substrates are shown in Figs. 3(a)–3(c), respectively. While the films grown on CGO and MGO exhibit sharp interfaces and are essentially free of APBs and other defects, the film grown on MAO presents many structural defects. These defects are clearly seen using the LAADF imaging mode, as shown in the lower panel of Fig. 3(c). The bright contrast of this image stems from crystal defects, mainly APBs,

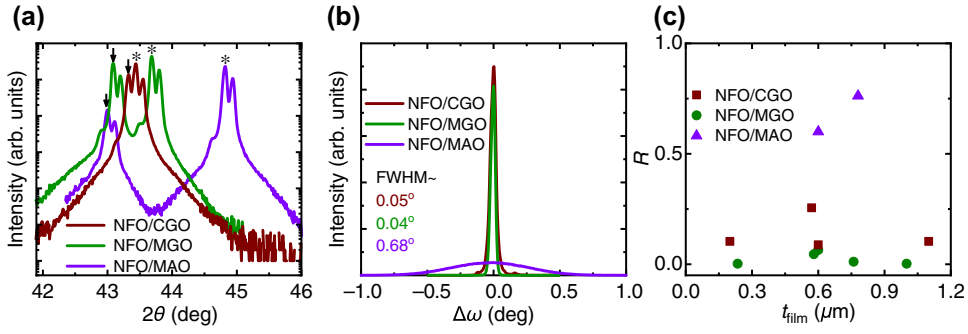

FIG. 2. (a) Standard θ-2θ diffraction patterns around the (004) reflections of the substrates (*) and films (↓), respectively. (b) The FWHM of omega scans of NFO films grown on the different substrates. (c) Variation of the strain parameter R with the thickness of NFO films deposited on the different substrates. The films on the MAO substrate are closer to being relaxed.

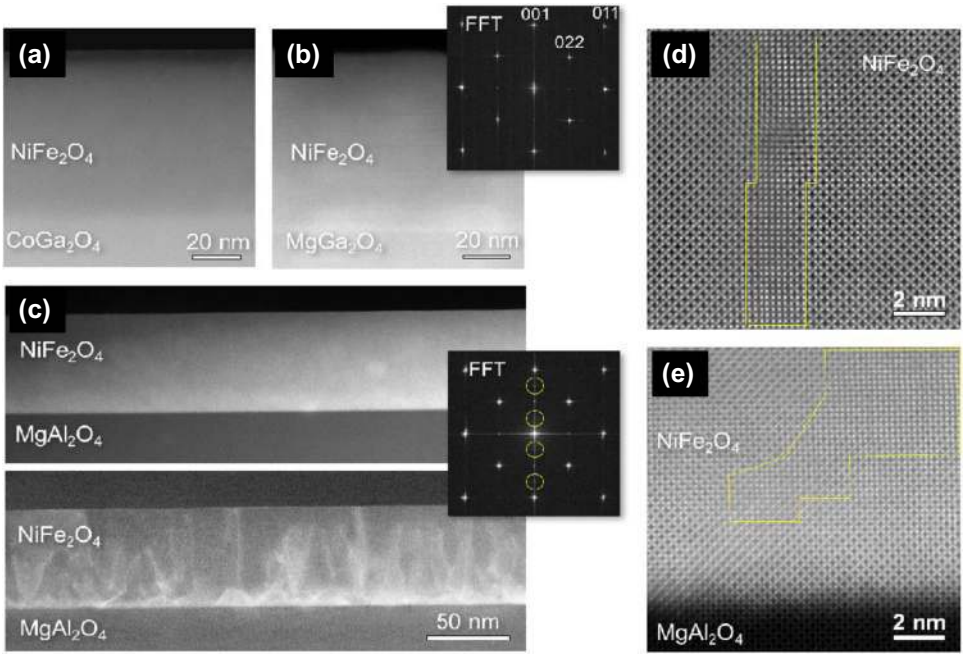

FIG. 3. (a),(b) Low magnification HAADF Z-contrast images of NFO films (approxiamtely 60 nm) grown on CGO and MGO substrates, respectively. The inset shows a characteristic FFT pattern from the *Z*-contrast image of (b). (c) Upper and lower panels show low magnification *Z*-contrast and LAADF images of NFO films grown on MAO, respectively. The inset shows an FFT of the NFO film grown on the MAO substrate. The yellow circles highlight the extra reflections arising due to the APBs. High-resolution *Z*-contrast images of an APB within the bulk of the film (d) and close to the interface (e) of the NFO films grown on MAO. APBs are highlighted in yellow.

with a crystallographic translation of $1/4a$ [001]. In high-resolution STEM *Z*-contrast images they appear with a clear distinct contrast, as highlighted in Figs. 3(d) and 3(e). These defects also appear as a superstructure in fast Fourier transform (FFT) patterns, as shown in the FFT of an NFO film grown on the MAO substrate [inset Fig. 3(c)]. The extra reflections marked with yellow circles in the FFT are due to the presence of APBs, and are absent in the FFT patterns of NFO films grown on CGO and MGO substrates [inset Fig. 3(b)]. The LAADF image also shows that the defects are unevenly distributed, as the density of APBs decreases near the surface of the film. Our previous studies have established that even relatively thick NFO films (100–450 nm) grown on CGO and MGO substrates remain essentially fully strained while those on MAO are partially relaxed with formation of misfit dislocations [29]. This is consistent with the x-ray diffraction results. The films on MAO also show the presence of threading dislocation and dark diffused contrast areas, likely from A-site cation vacancies [27,29]. The APBs and other structural defects are known to cause a reduction of saturation magnetization and increase in the FMR linewidth of the thin films compared to their bulk values [40]. However, their effect on the spin-transport properties and especially on ISHE remain unknown.

B. Spin Seebeck effect measurements of NFO films on different substrates

In Fig. 4(a), we show a schematic of the measurement geometry for LSSE. The temperature gradient across the film and the substrate is simulated using the heat-transfer module and finite-element method available in COMSOL Multiphysics®. The simulation for a 330-nm NFO film on the MGO substrate is shown in Figs. 4(b) and 4(c). The temperature gradient (ΔT_f) is in the range of tens of mK/μm when a temperature difference of approximately 20 K is applied across the Cu blocks. Figure 4(b) shows the cross-section view of temperature distribution across the stack. For clarity, the temperature profile across the film is shown in the enlarged cross-section image [Fig. 4(c)]. Further details are provided in Sec. I of the SM [39,41–43]. We find that the temperature difference across the film scales with the temperature difference across the Cu blocks and is essentially independent of the choice of the substrate (MAO, MGO, and CGO) because of their similar thermal characteristics (see Table I within the SM [39]).

In our geometry we are sensitive to the $\hat{x}$ component of $\mathbf{E}_{\mathrm{ISHE}}$ (with $V_{\mathrm{ISHE}} = E_{\mathrm{ISHE}}\, w$, w is the distance between voltage probes), and according to Eq. (1) we are sensitive to the $\hat{y}$ component of $\boldsymbol{\sigma}$ and thus $\mathbf{M}$. The background signal is subtracted from data presented here (for raw data please see Fig. S3 within the SM [39]). In Fig. 4(d), we display the result for a 330-nm-thick NFO/MGO film with angular variation from 0° to 90° between the voltage contacts and the magnetic field. We observe that upon reversing the direction of ΔT_z, the voltage signal is also reversed, which is a characteristic behavior of V_{ISHE} induced by LSSE (see Fig. S4 within the SM [39]). To obtain the maximum LSSE voltage the external magnetic field is applied along the $\hat{y}$ direction ($\theta = 90°$) to saturate the magnetization aligned along this direction. This leads to a maximum V_{sat} of approximately 27 μV. After magnetic field reversal, the magnetization direction is changed into the opposite direction and V_{sat} of approximately -27 μV is obtained. During the magnetic field reversal process [Fig. 4(d)], V_{LSSE} acts in correspondence with the magnetization and

correlates well with the VSM measurement (see Fig. S5 within the SM [39]). When θ is reduced, V_{sat} decreases and follows the cross product of Eq. (1), which is evident from Fig. 4(e). During the magnetic field reversal process, the magnetization rotates towards one of the magnetic easy axes aligned along 45° in [011] directions [44]. For angles $\theta > 45°$ upon reducing the magnetic field, the projection of the magnetization onto the $\hat{y}$ direction also decreases, which results in a decrease of V_{LSSE}. For $\theta = 45°$, V_{LSSE} signal shows the maximum squareness while the magnetization lies along one of the magnetic easy axes. For angles $\theta < 45°$, V_{LSSE} signal increases when the magnetic field is decreased due to the increase of the projection of the magnetization in the $\hat{y}$ direction. Across $H = 0$ Oe, **M** lies along one of the magnetic easy axes and results in nearly the same remanent voltage signal for all angles θ (see Fig. S6 within the SM [39]). For $\theta \leq 30°$ we observe a slight difference around $H = 0$ Oe, which can be attributed due to the multidomain formation during the reversal process [45]. We additionally perform magnetic and LSSE measurements on an NFO film grown on (011)-oriented MGO substrate (see details in the Appendix and the results in Ref. [46]).

The temperature dependence (from 30 to 300 K) of normalized LSSE voltage for 330-nm-thick films is shown in Fig. 4(f), with the ΔT across the stack being fixed at 20 K. This observation is similar to the results for CVD-deposited NFO films on the MAO substrate [12]. In some previous reports, the temperature dependence of the ISHE signal has been discussed for magnetic insulator-normal metal hybrid structures [47–49]. A $T^{3/2}$ variation at low temperatures has been theoretically proposed, [47,48], while a $(T_c - T)^3$ (T_c is the Curie temperature) dependence at higher temperatures has been experimentally observed for Pt/YIG [49]. We combine these two temperature regimes and fit our data [Fig. 4(f)] with $V_{LSSE} \propto T^{3/2}(T_c - T)^3$. This relationship fits well with our observation in the measured temperature range. From the fits, T_c is found to be in the range 700–800 K, which is close to the NFO bulk value (approximately 850 K) [50].

In Fig. 5(a), we plot the magnetic field variation of the SSE voltage of 600-nm-thick films on MGO (circle), CGO (square), and MAO (triangle) obtained using the heat-flux method. Here the V_{LSSE} signal of the film on MGO is larger as compared to CGO. On the other hand, SSE voltage across the films on the MAO substrate remains lowest in both the measurement techniques, which is evident from Figs. 4(e) and 5(a). In Fig. 5(b), we show the variation of normalized saturation electric field (E_c) generated in the Pd layer as a function of the lattice mismatch with the three

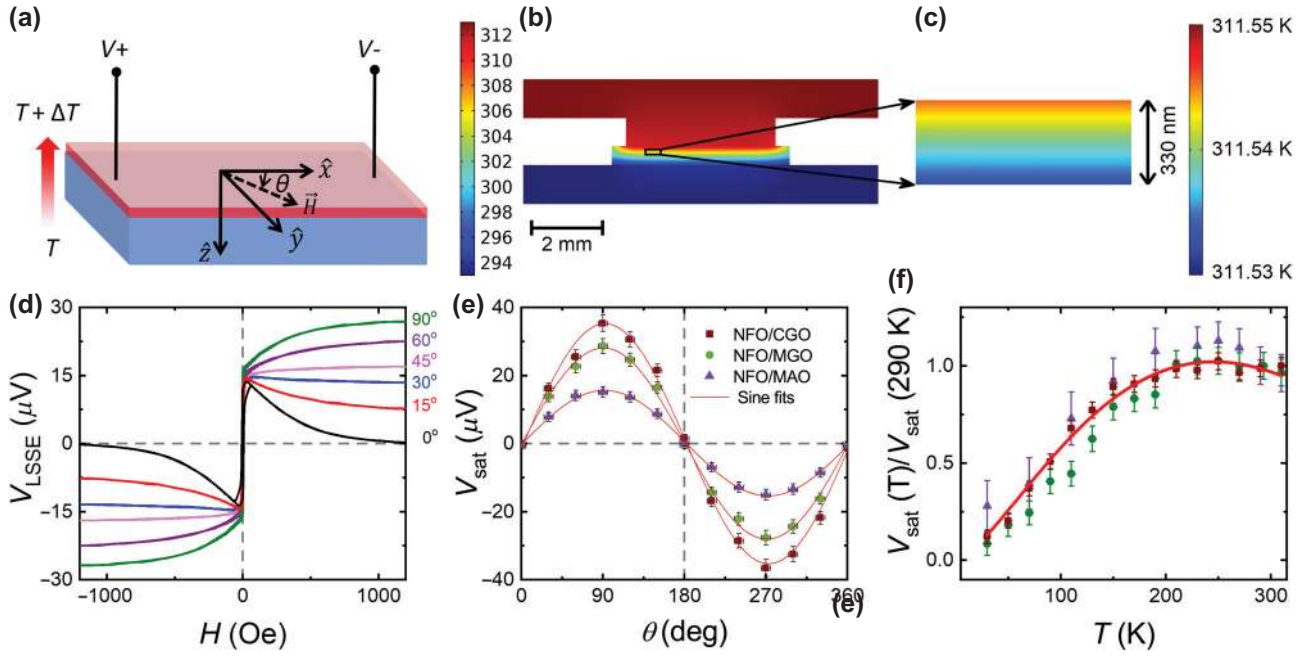

FIG. 4. (a) Schematic of the LSSE measurement geometry. A temperature gradient is created along the $\hat{z}$ direction; the magnetic field is applied in the sample plane with an angle θ with respect to the $\hat{x}$ direction, and the voltage is measured in the same plane. (b),(c) Results of COMSOL Multiphysics® simulation for the generation of the temperature gradient across the sample and the heating components. The film thickness is approximately 330 nm. (d) LSSE measurements for Pd/NFO/MGO (001) with voltage contacts located along the $\hat{x}$ direction and the external magnetic field applied in plane at various angles with respect to the voltage contacts. A complete angular dependence of the saturation voltage for all three films (330 nm) is plotted in (e); the dotted lines are sine-function fits. (f) Variation of normalized voltage signal $[V_{sat}(T)/V_{sat}(290\ K)]$ with various base temperatures (T) for 330-nm-thick films on different substrates. The solid line is the fit to the NFO and CGO data using Eq. (1) described in the text.

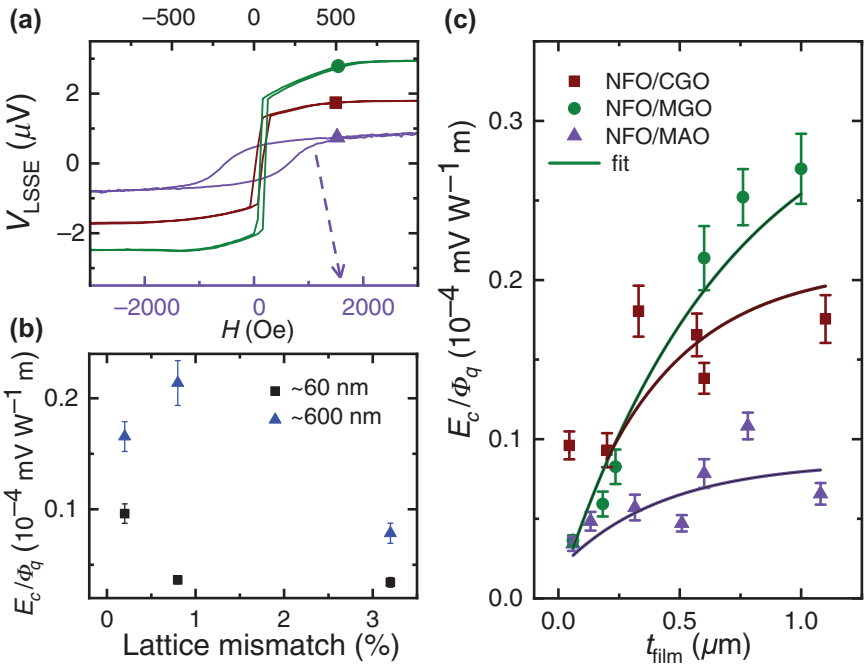

FIG. 5. (a) Magnetic field dependence of spin-voltage signal generated at constant heat flux (approxiamtely 24 kW/m^2) for three Pd/NFO films (600 nm) on different substrates. (b) Influence of lattice mismatch of NFO film with CGO, MGO, and MAO substrates for two different film thicknesses. (c) Thickness dependence for films on different substrates (symbols), while solid lines are fit to the equation $E_{LSSE} \propto 1 - \exp(-t_{film}/\xi)$, ξ is the magnon propagation length [51]. All measurements are performed using the heat-flux method at room temperature.

substrates. We observe a weak SSE signal for films grown on the MAO substrate and larger SSE response for NFO films on MGO and CGO. Overall, it is noted that irrespective of the thickness of the films, the MAO substrate shows the lowest LSSE signal. This signifies the importance of lattice mismatch in enhancing the E_c/Φ_q signal. In conjunction with the STEM results we conclude that APBs and other structural defects present in the films are one of the reasons associated with the change in the LSSE signal. The values of E_c/Φ_q for Pd/NFO/MGO are in a similar range (approximately 30 nm/A) as recently reported for Pt/YIG/GGG thin film heterostructure (approximately 40 nm/A) [52]. Here, the effect of the lower spin Hall angle of Pd [30–32] is probably compensated by a larger SSE in the NFO. If directly compared to sputter-deposited Pt/NFO bilayers (approximately 100 nm/A) [19], the effect of less efficient spin-to-charge conversion in Pd becomes obvious. However, complete SSE thickness dependencies are quite rare in the literature, especially when normalized to the heat flux, and should be investigated in future studies. Finally, since the spin Seebeck resistivity E_c/Φ_q is only an effective SSE coefficient that still includes the heat conductivity of the NFO, any thickness-dependent change of the NFO heat conductivity can affect the thickness dependence of the heat-flux-normalized SSE voltages. The study of this dependence will be part of future work.

Our measurements show an increase in normalized saturation electric field (E) generated across the Pd layer by the heat flux (Φ_q) with increasing film thickness [Fig. 5(c)], which can be explained based on characteristic magnon propagation length (ξ), i.e., the number of magnons reaching the Pd-ferrimagnetic interface increases with thickness [51–53] and contributes to the voltage signal. The value of ξ deduced from the fits is in the range of 400–700 nm. This is lower than the recently reported value obtained from nonlocal magnon spin-transport measurements in sputter-deposited NFO films (approximately 3 μm) [26,54]. Such a discrepancy between local LSSE and nonlocal magnon spin-transport results has also been observed for YIG [28,51] and can be explained by the different nature of the experiments. While magnons with different propagation lengths can reach the Pd interface in the local experiment, the magnons with small diffusion length cannot make it to the Pd detector in the nonlocal geometry. Upon further increasing the film thickness, we observe an increase and saturation in the voltage signal. Significant scatter is observed in the data points for the films on CGO. This might be due to differences in the quality of CGO substrates, which is also reflected in FMR measurements, where we find scatter in the FMR linewidth (see Fig. S8 within the SM [39]).

C. FMR measurements of NFO films on different substrates

In addition to the LSSE measurements, we compare the dynamical properties of NFO films (330 nm) deposited on CGO and MGO substrates by FMR in the field along the in-plane magnetic hard-axis geometry. From the measurements, we estimate the effective magnetization (M_{eff}) and gyromagnetic ratio (γ') from fitting the frequency (f) versus resonance field (H_{res}) data [Fig. 6(a)] to the Kittel

equation in the in-plane configuration using equation

$$f = \gamma' \sqrt{(H_{\text{res}} + H_4)(H_{\text{res}} + H_4 + 4\pi M_{\text{eff}})}, \qquad (2)$$

where H_4 is the fourfold in-plane anisotropy. The FMR linewidth (ΔH) versus frequency (f) data is then used to calculate the effective Gilbert damping parameter (α_{eff}) and inhomogeneous linewidth broadening (ΔH_0) from the equation [55,56]

$$\Delta H = \Delta H_0 + \frac{2\alpha_{\text{eff}}}{\sqrt{3}\gamma'} f\,. \qquad (3)$$

Linewidth versus frequency data is shown in Fig. 6(b) for 330-nm-thick NFO films on MGO and CGO substrates with the Pd top layer. The estimated value of the α_{eff} of the NFO/MGO and NFO/CGO thin films without the Pd top layer are determined to be $(22 \pm 0.9) \times 10^{-4}$ and $(1.3 \pm 0.9) \times 10^{-4}$, respectively (see Fig. S9 within the SM [39]). After Pd deposition we find an increase in the damping constant and the effective Gilbert damping parameter. The values derived from the fitting of the data in Fig. 6(b) are $(2.9 \pm 0.1) \times 10^{-3}$ and $(2.3 \pm 0.1) \times 10^{-3}$ for the Pd/NFO/MGO and Pd/NFO/CGO films, respectively. The difference in the Gilbert damping parameter of the two films capped with and without Pd can be directly related to the spin current density in the two films which can explain the significant differences in the SSE voltage for the two films [57]. It should be noted that the value of α_{eff} for NFO/CGO [$(1.3 \pm 0.9) \times 10^{-4}$] is comparable to the best reported value of YIG/GGG thin films (approximately 7.35×10^{-5}) [17], suggesting that NFO/CGO is a promising candidate for spin caloritronics and spin transport in general. Furthermore, to estimate the spin-mixing conductance $g_{\uparrow\downarrow}$ from FMR spin damping results, we use the equation [58]

$$g_{\uparrow\downarrow} = \frac{4\pi M_s\, t_{\text{NFO}}}{g\mu_B} \left(\alpha_{\text{Pd/NFO}} - \alpha_{\text{NFO}}\right), \qquad (4)$$

where $4\pi M_s$, t_{NFO}, g, μ_B, $\alpha_{\text{Pd/NFO}}$, and α_{NFO} are NFO saturation magnetization, film thickness, Landé g factor, Bohr magneton, and effective Gilbert damping constants of Pd/NFO and pure NFO, respectively. Based on the values provided in our manuscript, $g_{\uparrow\downarrow}$ for Pd(5 nm)/NFO(330 nm)/CGO is estimated to be approximately $2.1 \times 10^{-17}\,\text{m}^{-2}$, which is somewhat higher than the value of $g_{\uparrow\downarrow}$ (approximately $6.9 \times 10^{-18}\,\text{m}^{-2}$) for Pt(5 nm)/YIG(20 nm)/GGG reported in the literature [58].

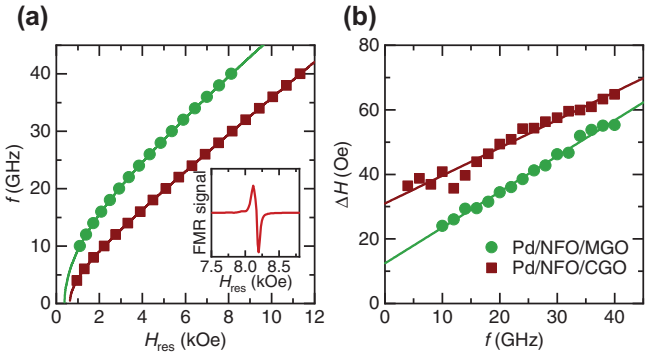

FIG. 6. Broadband FMR measurement results of 330-nm-thick NFO films with the Pd top layer deposited on CGO and MGO substrates. (a) Microwave frequency versus resonance-field data (symbols) are fitted to the Kittel equation (solid lines). The inset shows a typical FMR spectra of the film at 30-GHz frequency. (b) The dependence of FMR linewidth signal with resonance frequency (solid data points) and solid lines are fits to calculate the effective Gilbert damping and inhomogeneous linewidth broadening.

IV. CONCLUSIONS

In summary, thin films of NFO exhibit improved structural, interfacial, and dynamical properties when grown on lattice-matched substrates. The results clearly show that higher LSSE signal is obtained for the most closely lattice-matched substrates (MGO, CGO). We find that the thinner films on the CGO substrate provide larger LSSE voltage signal as compared to the other heterostructures and this is consistent with the lower value of the effective Gilbert damping of these films. COMSOL Multiphysics® simulation indicates that the temperature gradient across the film is in the range of tens of mK/μm. The measurements using the heat-flux method also affirm the importance of lattice matching to enhance spin-generated voltage signal that also correlates with the FMR results. Apart from this, LSSE measurements provide a qualitative method to study in-plane magnetic anisotropies by varying the angle between the external magnetic field and the direction of the contacts for the detection of the ISHE voltage. Improved quality NFO thin films exhibit a damping parameter comparable to that of YIG/GGG, which makes them attractive for spintronics as well as microwave applications. Further improvement of the LSSE efficiency of NFO can be realized by choosing substrates with even less lattice mismatch compared to MGO and CGO.

ACKNOWLEDGMENTS

The work at The University of Alabama is supported by NSF ECCS Grant No. 1509875 and NSF CAREER Award No. 0952929. The work at ORNL (A.Y.B.) is supported by the Materials Science and Engineering Division of the Office of Science of the US DOE. R.M. acknowledges support from NSF through Grant No. DMR-1809571. J.G. is supported by the Ramón y Cajal program (RyC-2012-11709). J.G. also acknowledges financial support from the Spanish Ministry of Science Innovation and Universities through the 'Severo Ochoa' Programme for Centres of Excellence in R&D (SEV-2015- 0496). The Bielefeld

group (T.P., B.P., D.M., G.R., T.K.) gratefully acknowledge financial support by the Deutsche Forschungsgemeinschaft (DFG) within the priority program Spin Caloric Transport (SPP 1538).

A.R. and Z.L. contributed equally to this work.

APPENDIX: SPIN SEEBECK MEASUREMENTS OF NFO FILMS GROWN ON (011)-ORIENTED MGO SUBSTRATES

Magnetization measurements are performed on a 330-nm-thick $NiFe_2O_4$ film grown on (011)-oriented $MgGa_2O_4$ substrate to examine the in-plane magnetic anisotropy. As shown in Fig. 7(a), we observe a sharp switching of the magnetization when the external magnetic field is applied along the magnetic easy axis [01$\bar{1}$], with a squareness of approximately one. With the external magnetic field applied along the magnetic hard axis ([100]), we obtain switching behavior associated with a magnetic hard axis with an anisotropy field of about 2000 Oe, and squareness far less than one. We measure the V_{ISHE} signal in two configurations. In the first configuration the V_{ISHE} signal is measured along the magnetic hard axis of the $NiFe_2O_4$ film, i.e., along the $\hat{y}$ direction [Fig. 7(b)], and in the other case the V_{ISHE} signal is measured along the magnetic easy axis, i.e., along the $\hat{x}$ direction [Fig. 7(c)].

In the first configuration, we measure the voltage signal along the magnetic hard axis, i.e., along the [100] direction. When the magnetic field is applied along the magnetic easy axis, i.e., along the [01$\bar{1}$] direction, the magnetization of the $NiFe_2O_4$ film also aligns along the same direction and when the magnetic field direction changes polarity the magnetization switches into the opposite direction. This results in a sharp switching in the V_{ISHE} signal [90° in Fig. 7(b)] and it is comparable to the corresponding magnetization measurement when the magnetic field is applied in the [01$\bar{1}$] direction [Fig. 7(a)]. In the next step, we change the angle θ of the external magnetic field with respect to the voltage-measurement direction, i.e., from the $\hat{y}$ direction in the range from 0° to 90°. In saturation, the magnetization of the $NiFe_2O_4$ is aligned along the direction of the external magnetic field for all θ angles. The direction of the voltage measurement is only sensitive for the detection of the spin current that is spin polarized along the $\hat{x}$ direction. The voltage generation due to ISHE arises from the projection of the magnetization in the $\hat{x}$ direction. Upon lowering the angle between the external magnetic field and the $\hat{y}$ direction, the saturation voltage decreases in correspondence with the cross product in the ISHE equation. When the magnetic field decreases, the magnetization rotates coherently into the magnetic easy axis. The projection of the magnetization in the $\hat{x}$ direction increases, which also increases the measured voltage by the ISHE. At zero magnetic field the magnetization rotates completely into the magnetic easy axis. This occurs for all angles θ up to 15°, which results in nearly the same voltage signal. Subsequently, when the magnetic field polarity is changed the magnetization switches into the opposite direction along the magnetic easy axis. Upon increasing the magnetic field in the negative direction the measured voltage decreases in corresponding to a coherent rotation of the magnetization into the magnetic field direction. For lower angles θ, the magnetization switching deviates more and more from the sharp switching behavior observed for larger angles. For 15° and 0°, i.e., near the magnetic hard axis, we observe a behavior corresponding to the presence of multiple domains. The domains rotate clockwise or counterclockwise into the next magnetic easy axis. This leads to an intermediate voltage for 0° around zero magnetic field, which is smaller than the observed value when all domains rotate into the same direction.

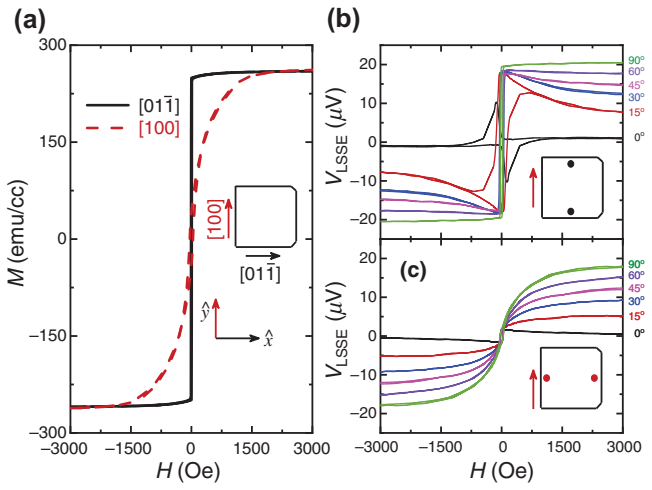

FIG. 7. (a) Variation of magnetization with magnetic field for a 330-nm-thick NFO/MGO (011) film. The magnetization is measured with the external in-plane magnetic field applied in the direction of the magnetic easy axis [01$\bar{1}$] (black line) and the magnetic hard axis [100] (red line), respectively. LSSE measurements at various angles for Pd/NFO/MGO with voltage being measured (b) along the [100] direction and (c) along the [01$\bar{1}$] direction, respectively.

In the second configuration, we change the position of the voltage contacts and measured the V_{ISHE} signal along the magnetic easy axis. When the external magnetic field is applied along the magnetic hard axis to complete the typical LSSE configuration, i.e., $\theta = 90°$, we observe an LSSE voltage curve similar to the magnetization curve along the magnetic hard axis ([100] direction in Fig. 7(a)). The LSSE signal saturates at the highest applied external magnetic field. When the external magnetic field is reduced the LSSE voltage does not show a sharp switching, but favors the curved shape of the magnetization measurement in the [100] direction with low remanence. While the projection of the magnetization into the $\hat{y}$ direction decreases

monotonically, the LSSE voltage also decreases. After changing the polarity of the magnetic field, the magnetization switches by 180° into the magnetic easy axis, which is along the voltage contacts. This results in a nearly zero voltage signal. When the magnetic field increases again in the negative direction, the magnetization rotates back into the magnetic field direction. The projection into the $\hat{y}$ direction as well as the absolute value of the V_{ISHE} increases, because the electric field along the voltage contacts increases due to the ISHE. The saturation voltage follows, again, the cross product of the ISHE and can be compared to the saturated voltage in Fig. 7(b). The slight differences can be explained by misalignments of the voltage contacts and the direction of the magnetic field. For angles θ larger than 0° [Fig. 7(c)], the saturation voltage increases (decreases) for positive (negative) magnetic fields similar to the configuration in Fig. 7(b). When the magnetic field is reduced the curves for θ between 15° and 60° can be explained in the same manner as for $\theta = 90°$. For $\theta = 0°$ the saturation voltage is nearly zero as expected, but around zero magnetic field the measured voltage increases (decreases) when the external magnetic field is decreased (increased). Here, we expect an accurate alignment with the voltage contacts, but a misalignment of the voltage contacts with respect to the magnetic easy axis. This results in a slight voltage contribution at zero field when the magnetization rotates into the magnetic easy axis. The LSSE measurements provide an attractive alternative to investigate in-plane magnetic anisotropies by varying the direction of the voltage contacts and the angle of the external magnetic field. The alignment accuracy between the voltage contacts, and the external magnetic field with respect to the magnetic easy axis can in principle be controlled very precisely. This kind of vectorial magnetometry based on LSSE measurements has been described in detail in Ref. [46].

[1] S. A. Wolf, D. D. Awschalom, R. A. Buhrman, J. M. Daughton, S. von Molnár, M. L. Roukes, A. Y. Chtchelkanova, and D. M. Treger, Spintronics: A spin-based electronics vision for the future, Science **294**, 1488 (2001).

[2] I. Žutić, J. Fabian, and S. Das Sarma, Spintronics: Fundamentals and applications, Rev. Mod. Phys. **76**, 323 (2004).

[3] G. E. W. Bauer, E. Saitoh, and B. J. van Wees, Spin caloritronics, Nat. Mater. **11**, 391 (2012).

[4] A. Kirihara, K.-i. Uchida, Y. Kajiwara, M. Ishida, Y. Nakamura, T. Manako, E. Saitoh, and S. Yorozu, Spin-current-driven thermoelectric coating, Nat. Mater. **11**, 686 (2012).

[5] K.-i. Uchida, A. Kirihara, M. Ishida, R. Takahashi, and E. Saitoh, Local spin-Seebeck effect enabling two-dimensional position sensing, Jpn. J. Appl. Phys. **50**, 120211 SEP (2011).

[6] S. R. Boona, R. C. Myers, and J. P. Heremans, Spin caloritronics, Energy Environ. Sci. **7**, 885 (2014).

[7] K.-i. Uchida, H. Adachi, T. Kikkawa, A. Kirihara, M. Ishida, S. Yorozu, S. Maekawa, and E. Saitoh, Thermoelectric generation based on spin Seebeck effects, Proc. IEEE **104**, 1946 (2016).

[8] K. Uchida, S. Takahashi, K. Harii, J. Ieda, W. Koshibae, K. Ando, S. Maekawa, and E. Saitoh, Observation of the spin Seebeck effect, Nature **455**, 778 (2008).

[9] S. Bosu, Y. Sakuraba, K. Uchida, K. Saito, T. Ota, E. Saitoh, and K. Takanashi, Spin Seebeck effect in thin films of the Heusler compound Co_2MnSi, Phys. Rev. B **83**, 224401 (2011).

[10] C. M. Jaworski, J. Yang, S. Mack, D. D. Awschalom, J. P. Heremans, and R. C. Myers, Observation of the spin-Seebeck effect in a ferromagnetic semiconductor, Nat. Mater. **9**, 898 (2010).

[11] H. Adachi, K.-i. Uchida, E. Saitoh, J.-i. Ohe, S. Takahashi, and S. Maekawa, Gigantic enhancement of spin Seebeck effect by phonon drag, Appl. Phys. Lett. **97**, 252506 (2010).

[12] D. Meier, T. Kuschel, L. Shen, A. Gupta, T. Kikkawa, K. Uchida, E. Saitoh, J. M. Schmalhorst, and G. Reiss, Thermally driven spin and charge currents in thin $NiFe_2O_4$/Pt films, Phys. Rev. B **87**, 054421 (2013).

[13] S. O. Valenzuela and M. Tinkham, Direct electronic measurement of the spin Hall effect, Nature **442**, 176 (2006).

[14] E. Saitoh, M. Ueda, H. Miyajima, and G. Tatara, Conversion of spin current into charge current at room temperature: Inverse spin-Hall effect, Appl. Phys. Lett. **88**, 182509 (2006).

[15] T. Kimura, Y. Otani, T. Sato, S. Takahashi, and S. Maekawa, Room-Temperature Reversible Spin Hall Effect, Phys. Rev. Lett. **98**, 156601 (2007).

[16] S. Y. Huang, W. G. Wang, S. F. Lee, J. Kwo, and C. L. Chien, Intrinsic Spin-Dependent Thermal Transport, Phys. Rev. Lett. **107**, 216604 (2011).

[17] C. Hauser, T. Richter, N. Homonnay, C. Eisenschmidt, M. Qaid, H. Deniz, D. Hesse, M. Sawicki, S. G. Ebbinghaus, and G. Schmidt, Yttrium iron garnet thin films with very low damping obtained by recrystallization of amorphous material, Sci. Rep. **6**, 20827 (2016).

[18] C. N. Chinnasamy, S. D. Yoon, A. Yang, A. Baraskar, C. Vittoria, and V. G. Harris, Effect of growth temperature on the magnetic, microwave, and cation inversion properties on $NiFe_2O_4$ thin films deposited by pulsed laser ablation deposition, J. Appl. Phys. **101**, 09M517 (2007).

[19] P. Bougiatioti, C. Klewe, D. Meier, O. Manos, O. Kuschel, J. Wollschlaeger, L. Bouchenoire, S. D. Brown, J.-M. Schmalhorst, G. Reiss, and T. Kuschel, Quantitative Disentanglement of the Spin Seebeck, Proximity-Induced, and Ferromagnetic-Induced Anomalous Nernst Effect in Normal-Metal-Ferromagnet Bilayers, Phys. Rev. Lett. **119**, 227205 (2017).

[20] P. Bougiatioti, O. Manos, C. Klewe, D. Meier, N. Teichert, J.-M. Schmalhorst, T. Kuschel, and G. Reiss, Electrical transport and optical band gap of $NiFe_2O_x$ thin films, J. Appl. Phys. **122**, 225101 (2017).

[21] D. Meier, D. Reinhardt, M. van Straaten, C. Klewe, M. Althammer, M. Schreier, S. T. B. Goennenwein, A. Gupta,

M. Schmid, C. H. Back, J.-M. Schmalhorst, T. Kuschel, and G. Reiss, Longitudinal spin Seebeck effect contribution in transverse spin Seebeck effect experiments in Pt/YIG and Pt/NFO, Nat. Commun. **6**, 8211 (2015).

[22] D. Meier, T. Kuschel, S. Meyer, S. T. Goennenwein, L. Shen, A. Gupta, J.-M. Schmalhorst, and G. Reiss, Detection of DC currents and resistance measurements in longitudinal spin Seebeck effect experiments on Pt/YIG and Pt/NFO, AIP Adv. **6**, 056302 (2016).

[23] T. Kuschel, C. Klewe, J. M. Schmalhorst, F. Bertram, O. Kuschel, T. Schemme, J. Wollschlaeger, S. Francoual, J. Strempfer, A. Gupta, M. Meinert, G. Goetz, D. Meier, and G. Reiss, Static Magnetic Proximity Effect in $Pt/NiFe_2O_4$ and Pt/Fe Bilayers Investigated by X-Ray Resonant Magnetic Reflectivity, Phys. Rev. Lett. **115**, 097401 (2015).

[24] C. Klewe, M. Meinert, A. Boehnke, K. Kuepper, E. Arenholz, A. Gupta, J.-M. Schmalhorst, T. Kuschel, and G. Reiss, Physical characteristics and cation distribution of $NiFe_2O_4$ thin films with high resistivity prepared by reactive co-sputtering, J. Appl. Phys. **115**, 123903 (2014).

[25] T. Kuschel, C. Klewe, P. Bougiatioti, O. Kuschel, J. Wollschlaeger, L. Bouchenoire, S. D. Brown, J.-M. Schmalhorst, D. Meier, and G. Reiss, Static magnetic proximity effect in Pt layers on sputter-deposited $NiFe_2O_4$ and on Fe of various thicknesses investigated by XRMR, IEEE Trans. Magn. **52**, 4500104 (2016).

[26] J. Shan, P. Bougiatioti, L. Liang, G. Reiss, T. Kuschel, and B. J. van Wees, Nonlocal magnon spin transport in $NiFe_2O_4$ thin films, Appl. Phys. Lett. **110**, 132406 (2017).

[27] N. Li, S. Schäfer, R. Datta, T. Mewes, T. Klein, and A. Gupta, Microstructural and ferromagnetic resonance properties of epitaxial nickel ferrite films grown by chemical vapor deposition, Appl. Phys. Lett. **101**, 132409 (2012).

[28] L. J. Cornelissen, J. Liu, R. A. Duine, J. B. Youssef, and B. J. van Wees, Long-distance transport of magnon spin information in a magnetic insulator at room temperature, Nat. Phys. **11**, 1022 (2015).

[29] A. V. Singh, B. Khodadadi, J. B. Mohammadi, S. Keshavarz, T. Mewes, D. S. Negi, R. Datta, Z. Galazka, R. Uecker, and A. Gupta, Bulk single crystal-like structural and magnetic characteristics of epitaxial spinel ferrite thin films with elimination of antiphase boundaries, Adv. Mater. **29**, 1701222 (2017).

[30] K. Ando and E. Saitoh, Inverse spin-Hall effect in palladium at room temperature, J. Appl. Phys. **108**, 113925 (2010).

[31] X. Tao, Q. Liu, B. Miao, R. Yu, Z. Feng, L. Sun, B. You, J. Du, K. Chen, S. Zhang, L. Zhang, Z. Yuan, D. Wu, and H. Ding, Self-consistent determination of spin Hall angle and spin diffusion length in Pt and Pd: The role of the interface spin loss, Sci. Adv. **4**, eaat1670 (2018).

[32] L. Ma, L. Lang, J. Kim, Z. Yuan, R. Wu, S. Zhou, and X. Qiu, Spin diffusion length and spin Hall angle in $Pd_{1-x}Pt_x$/YIG heterostructures: Examination of spin relaxation mechanism, Phys. Rev. B **98**, 224424 (2018).

[33] Z. Galazka, D. Klimm, K. Irmscher, R. Uecker, M. Pietsch, R. Bertram, M. Naumann, M. Albrecht, A. Kwasniewski, R. Schewski, and M. Bickermann, $MgGa_2O_4$ as a new wide bandgap transparent semiconducting oxide: growth and properties of bulk single crystals, Phys. Status Solidi A **212**, 1455 (2015).

[34] S. Pennycook and D. Jesson, High-resolution Z-contrast imaging of crystals, Ultramicroscopy **37**, 14 (1991).

[35] J. Cowley and Y. Huang, De-channelling contrast in annular dark-field STEM, Ultramicroscopy **40**, 171 (1992).

[36] A. Sola, M. Kuepferling, V. Basso, M. Pasquale, T. Kikkawa, K. Uchida, and E. Saitoh, Evaluation of thermal gradients in longitudinal spin Seebeck effect measurements, J. Appl. Phys. **117**, 17C510 (2015).

[37] A. Sola, P. Bougiatioti, M. Kuepferling, D. Meier, G. Reiss, M. Pasquale, T. Kuschel, and V. Basso, Longitudinal spin Seebeck coefficient: Heat flux vs. temperature difference method, Sci. Rep. **7**, 46752 (2017).

[38] A. Sola, V. Basso, M. Kuepferling, M. Pasquale, D. C. né Meier, G. Reiss, T. Kuschel, T. Kikkawa, K. Uchida, E. Saitoh, H. Jin, S. J. Watzman, S. Boona, J. Heremans, M. B. Jungfleisch, W. Zhang, J. E. Pearson, A. Hoffmann, and H. W. Schumacher, Spincaloritronic measurements: A round robin comparison of the longitudinal spin Seebeck effect, IEEE Trans. Instrum. Meas. **68**, 1765 (2019).

[39] See the Supplemental Material at http://link.aps.org/supplemental/10.1103/PhysRevApplied.14.014014 for the details of COMSOL Multiphysics® simulations, SSE measurements of NFO films on different substrates, and FMR measurements.

[40] L. Torres, M. Zazo, J. Iniguez, C. de Francisco, and J. Munoz, Effect of slowly relaxing impurities on ferrimagnetic resonance linewidths of single crystal nickel ferrites, IEEE Trans. Magn. **29**, 3434 (1993).

[41] COMSOL Multiphysics material library, https://www.comsol.com/material-library.

[42] A. T. Nelson, J. T. White, D. A. Andersson, J. A. Aguiar, K. J. McClellan, D. D. Byler, M. P. Short, and C. R. Stanek, Thermal expansion, heat capacity, and thermal conductivity of nickel ferrite ($NiFe_2O_4$), J. Am. Ceram. Soc. **97**, 1559 (2014).

[43] K. R. Wilkerson, J. D. Smith, T. P. Sander, and J. G. Hemrick, Solid solution effects on the thermal properties in the $MgAl_2O_4$–$MgGa_2O_4$ system, J. Am. Ceram. Soc. **96**, 859 (2013).

[44] N. Pachauri, B. Khodadadi, A. V. Singh, J. B. Mohammadi, R. L. Martens, P. R. LeClair, C. Mewes, T. Mewes, and A. Gupta, A comprehensive study of ferromagnetic resonance and structural properties of iron-rich nickel ferrite ($Ni_xFe_{3-x}O_4$, $x \leq 1$) films grown by chemical vapor deposition, J. Magn. Magn. Mater. **417**, 137 (2016).

[45] A. Kehlberger, G. Jakob, M. C. Onbasli, D. H. Kim, C. A. Ross, and M. Klaeui, Investigation of the magnetic properties of insulating thin films using the longitudinal spin Seebeck effect, J. Appl. Phys. **115**, 17C731 (2014).

[46] Z. Li, J. Krieft, A. V. Singh, S. Regmi, A. Rastogi, A. Srivastava, Z. Galazka, T. Mewes, A. Gupta, and T. Kuschel, Vectorial observation of the spin Seebeck effect in epitaxial $NiFe_2O_4$ thin films with various magnetic anisotropy contributions, Appl. Phys. Lett. **114**, 232404 (2019).

[47] M. Weiler, M. Althammer, M. Schreier, J. Lotze, M. Pernpeintner, S. Meyer, H. Huebl, R. Gross, A. Kamra, J. Xiao, Y.-T. Chen, H. Jiao, G. E. W. Bauer, and S. T. B. Goennenwein, Experimental Test of the Spin Mixing Interface Conductivity Concept, Phys. Rev. Lett. **111**, 176601 (2013).

[48] M. Schreier, A. Kamra, M. Weiler, J. Xiao, G. E. W. Bauer, R. Gross, and S. T. B. Goennenwein, Magnon, phonon, and electron temperature profiles and the spin Seebeck effect in magnetic insulator/normal metal hybrid structures, Phys. Rev. B **88**, 094410 (2013).

[49] K.-i. Uchida, T. Kikkawa, A. Miura, J. Shiomi, and E. Saitoh, Quantitative Temperature Dependence of Longitudinal Spin Seebeck Effect at High Temperatures, Phys. Rev. X **4**, 041023 (2014).

[50] U. Lüders, A. Barthelemy, M. Bibes, K. Bouzehouane, S. Fusil, E. Jacquet, J.-P. Contour, J.-F. Bobo, J. Fontcuberta, and A. Fert, $NiFe_2O_4$: A versatile spinel material brings new opportunities for spintronics, Adv. Mater. **18**, 1733 (2006).

[51] A. Kehlberger, U. Ritzmann, D. Hinzke, E.-J. Guo, J. Cramer, G. Jakob, M. C. Onbasli, D. H. Kim, C. A. Ross, M. B. Jungfleisch, B. Hillebrands, U. Nowak, and M. Klaeui, Length Scale of the Spin Seebeck Effect, Phys. Rev. Lett. **115**, 096602 (2015).

[52] A. Prakash, B. Flebus, J. Brangham, F. Yang, Y. Tserkovnyak, and J. P. Heremans, Evidence for the role of the magnon energy relaxation length in the spin Seebeck effect, Phys. Rev. B **97**, 020408 (2018).

[53] U. Ritzmann, D. Hinzke, and U. Nowak, Propagation of thermally induced magnonic spin currents, Phys. Rev. B **89**, 024409 (2014).

[54] J. Shan, A. Singh, L. Liang, L. Cornelissen, Z. Galazka, A. Gupta, B. van Wees, and T. Kuschel, Enhanced magnon spin transport in $NiFe_2O_4$ thin films on a lattice-matched substrate, Appl. Phys. Lett. **113**, 162403 (2018).

[55] C. K. Mewes and T. Mewes, *Handbook of Nanomagnetism: Applications and Tools* (Pan Stanford Publishing, Singapore, 2015).

[56] H. Lee, L. Wen, M. Pathak, P. Janssen, P. LeClair, C. Alexander, C. Mewes, and T. Mewes, Spin pumping in $Co_{56}Fe_{24}B_{20}$ multilayer systems, J. Phys. D: Appl. Phys. **41**, 215001 (2008).

[57] H. Chang, P. A. P. Janantha, J. Ding, T. Liu, K. Cline, J. N. Gelfand, W. Li, M. C. Marconi, and M. Wu, Role of damping in spin Seebeck effect in yttrium iron garnet thin films, Sci. Adv. **3**, e1601614 (2017).

[58] H. Wang, C. Du, P. C. Hammel, and F. Yang, Comparative determination of $Y_3Fe_5O_{12}$/Pt interfacial spin mixing conductance by spin-Hall magnetoresistance and spin pumping, Appl. Phys. Lett. **110**, 062402 (2017).